ADVANCED FUNCTIONAL MATERIALS
www.afm-journal.de

Strategic Fabrication of Au_4Cu_2 NC/ZIF-8 Composite Via In Situ Integration Technique for Enhanced Energy Storage Applications

Muhammad Ahmad, Tehseen Nawaz, Yassine Eddahani, Iftikhar Hussain, Xi Chen, Kam Hung Low, Jian He,* and Kaili Zhang**

Metal–organic frameworks (MOFs), known for their extensive porosity and versatile crystallinity, play a crucial role in the development of advanced energy storage materials. However, their application is limited by stability and conductivity issues. This study addresses these challenges by integrating ultrasmall metal nanoclusters, specifically Au_4Cu_2 NC, synthesized using a mixed ligand strategy combining 2, 4-Dimethyl benzene thiol (2,4-DMBTH) and 1,2-bis(diphenylphosphino)ethane (dppe). The bimetallic Au_4Cu_2 NC, characterized by Single Crystal X-Ray Diffraction (SCXRD), is applied to zeolitic imidazolate framework-8 (ZIF-8) using both in situ and ex situ methods to explore their electrochemical and physicochemical properties in energy storage. The in situ Au_4Cu_2 NC/ZIF-8 composite demonstrated a specific capacitance that is almost two times higher than its ex situ counterpart, attributed to homogeneous dispersion and hence enhanced conductivity. This in situ integration of atomically precise bimetallic nanoclusters on MOFs significantly boosts supercapacitor performance, offering a more effective and reliable solution for energy storage. Further, in practical applications, this device demonstrated an energy density of 87.2 Wh kg^{-1} at a power density of 1474 W kg^{-1}, highlighting its robustness and potential for high-performance energy storage applications. This approach effectively combats the issue of nanocluster aggregation on substrates, marking a significant progression in supercapacitor technology.

1. Introduction

Metal–organic frameworks (MOFs), known for their highly porous crystalline structures, are at the forefront of creating cutting-edge materials.[1,2] These frameworks are marked for their chemical versatility and high porosity, which make them highly suitable for a range of uses, including energy storage and conversion technologies.[3,4] In the realm of supercapacitor (SC) electrode production, MOFs serve a dual role: as direct electrode materials and as templates for synthesizing various compounds. These compounds encompass porous carbons, metal oxides, metal sulfides, and metal phosphides, along with composite materials.[4,5] Despite these advantages, the direct use of MOFs in SC electrodes encounters hurdles, particularly due to their limited chemical stability and electrical conductivity. These limitations currently impede their widespread adoption in supercapacitor applications.[6–9]

Ultrasmall metal nanoclusters, with bridge gap between single atoms and

M. Ahmad, I. Hussain, X. Chen, K. Zhang
Department of Mechanical Engineering
City University of Hong Kong
83 Tat Chee Avenue, Kowloon, Hong Kong
E-mail: ihussaintoori1@gmail.com; kaizhang@cityu.edu.hk
M. Ahmad, Y. Eddahani
A.J. Drexel Nanomaterials Institute and Department of Materials Science and Engineering
Drexel University
3141 Chestnut Street, Philadelphia, Pennsylvania 19104, USA

The ORCID identification number(s) for the author(s) of this article can be found under https://doi.org/10.1002/adfm.202407059

DOI: 10.1002/adfm.202407059

T. Nawaz, K. H. Low, J. He
Department of Chemistry
The University of Hong Kong
Hong Kong, Hong Kong
E-mail: jianhe@hku.hk
I. Hussain, K. Zhang
Hong Kong Branch of Chinese National Engineering Research Centre (CNERC) for National Precious Metals Material (NPMM) Kowloon 999077 Hong Kong
83 Tat Chee Avenue, Hong Kong, Hong Kong 999077, Hong Kong

larger nanoparticles within the 1–3 nm size range, offer a promising avenue for exploration.[10–13] These clusters are encased in a stabilizing shell of protective ligands, which serves a dual purpose: it prevents the clusters from clumping together and significantly bolsters their stability.[14–16] The synthesis of new metal nanoclusters, characterized by their precise and intricately defined structures, has captured widespread interest, becoming a vibrant area of research in recent times.[17–24] Many researchers have put their efforts to investigate the chemical and atomic structures of metal nanocluster in last two decades. Qian et al.[25] explained the structural composition of an atomically precise nanocluster $Au_{38}(SCH_2CH_2Ph)_{24}$. This cluster composed of a central Au_{23} core, encircled by 3 monomeric [−SR−Au−SR−] staples, and further stabilized by 6 dimeric [−SR−Au−SR−Au−SR−] staples. The formation of alloy nanoclusters can be achieved by adding dopants to monometallic nanoclusters. Research has shown that incorporating heteroatoms, along with varying their quantity and spatial arrangement within the monometallic nanoclusters, can cause structural distortions. These changes are recognized for promoting improved charge dynamics within the clusters.[26,27] Metal nanoclusters tend to aggregate because of their high surface energy.[28,29] Providing a MOF substrate may facilitate to distribute the ultrasmall metal nanoclusters uniformly across the surface.

To date, the fabrication of stable atomically precise nanocluster/metal–organic framework composites has been confined to water-soluble atomically precise nanocluster, which are integrated into MOFs through coordination-assisted self-assembly,[30] and to negatively charged atomically precise nanocluster, which are coupled with MOFs via electrostatic attraction.[31] Recently, we have reported the synthesis of Ag-doped $Au_{38}(2,4\text{-DMBT})_{24}$ NCs, denoted as doped $Au_{38-x}Ag_x$ NCs protected by 24 2,4-DMBT ligands, and their applications in supercapacitors. The deposition of bimetallic nanocluster over ZIF-8 enhanced the conductivity of ZIF-8 significantly, consequently improved the specific capacitance of ZIF-8 by 3.64 times. However, the ex situ method of deposition of metal nanocluster on MOF directs to random and aggregated distribution on substrate surface.

Herein, we have integrated the atomically precise bimetallic Au_4Cu_2 nanocluster (NC) on ZIF-8 through in situ method. The atomically precise bimetallic Au_4Cu_2 nanocluster crystal structure was studied through single crystal XRD analysis. T in situ integration of Au_4Cu_2 nanocluster on ZIF-8 (in situ Au_4Cu_2 NC/ZIF-8) showed the excellent morphological characteristics such as uniformity of metal nanocluster over ZIF-8, in comparison to ex situ deposited metal nanocluster over ZIF-8 (Au_4Cu_2 NC@ZIF-8) analyzed by employing advanced morphological techniques. The in situ Au_4Cu_2 NC/ZIF-8 exhibited the outstanding conductivity, specific capacitance, and stability tests. Our comprehensive electrochemical and morphological analysis indicates that this innovative strategy of in situ integration of atomically precise bimetallic Au_4Cu_2 nanocluster on ZIF-8 could address the challenges of integration of metal nanocluster aggregation on substrate. The development of in situ Au_4Cu_2 NC/ZIF-8 represents a significant leap forward in the quest for efficient and sustainable supercapacitor technology.

2. Results and Discussion

The detailed synthesis methods are discussed in supplementary information. The synthesis of bimetallic Au_4Cu_2 NC was obtained through a co-reduction methodology involving the metal salts, $HAuCl_4{\cdot}3H_2O$ as Au source and $CuSO_4{\cdot}2H_2O$ as Cu source, with $NaBH_4$ in the presence of 2,4-DMBTH and dppe. A two-phase synthetic procedure was implicated at room temperature (Supporting Information). To investigate the precise molecular structure, the as synthesized product was developed into suitable dark crystals for SCXRD by slowly diffusing metanol into the dichloromethane solution at 4 °C (Figure S1, Supporting Information). Figure S1a (Supporting Information) illustrates the total structure of as prepared bimetallic NC.

The SCXRD analysis established that the nanocluster was crystallized in centrosymmetric monoclinic C 2/c space group where R = 6.13%. The structural exposition of the Au_4Cu_2 NC has shown a composition constituting four Au and two Cu atoms, which are stabilized by six 2,4-DMBT ligands and a singular dppe ligand as shown in Figure S1b,c (Supporting Information). This precise structure has been further supported by ESI-MS, a technique commonly applied for confirming the mass and structural composition of nanoclusters. The ESI-MS analysis has shown a predominant peak for the Au_4Cu_2 NC at m/z value of 2137.092 as shown in Figure S1d (Supporting Information). The precise match observed between the experimental and theoretical isotopic patterns has demonstrated the formulated structure of $Au_4Cu_2(2,4\text{-DMBT})_6$(dppe) cluster, as exhibited in **Figure 1**d (inset). UV–vis absorption spectra show that Au_4Cu_2 NC had characteristic absorption peaks at 324 and 394 nm as presented in Figure S1b (Supporting Information).

The intricate bimetallic framework within the Au_4Cu_2 NC is further described by the tricoordination of each copper atom with 2,4-DMBT ligands, with consequent development of a $Cu(SR)_3$ motif, as displayed in Figure 1a–c. Later analysis shows that the sulfur atoms within these tricoordinate moieties enable additional coordination to gold atoms as depicted in Figure 1a. Remarkably, two of the gold atoms act as junctures for the tricoordinate copper moieties, creating two [−SR−Au−SR−] staple motif (Figure 1b). Furthermore, the formation of Au_4Cu_2 NC was confirmed by high resolution transmission electron microscopy (HRTEM) as shown in Figure 1d,e. The Au_4Cu_2 NC were dispersed homogenously (Figure 1d). On closer inspection, it was discovered that the Au_4Cu_2 NC with a diameter of 1.83 nm exhibited quantum characteristics (with a size range of 4 nm) as depicted in Figure 1f. The close packing of Au_4Cu_2 NC in a unit cell is shown in Figure 1e.

Schematic illustration of in situ integrated Au_4Cu_2 NC/ZIF-8 and ex situ deposited Au_4Cu_2 NC@ZIF-8 is shown in **Figure 2**. The morphological analysis of the Au_4Cu_2 NC integration and deposition (in situ and ex situ, respectively) with ZIF-8 was evaluated using transmission electron microscopy (TEM), high-resolution transmission electron microscopy (HRTEM), high-angle annular dark-field (HAADF) imaging, and energy-dispersive X-ray spectroscopy (EDS) and shown in **Figure 3**. Figure 3a reveals the TEM images of the pristine ZIF-8, providing a baseline for comparison. Subsequently, Figure 3b–d presents the HRTEM and TEM images of the ex situ deposited in situ Au_4Cu_2 NC@ZIF-8 at varying magnifications. In Figure 3b, we

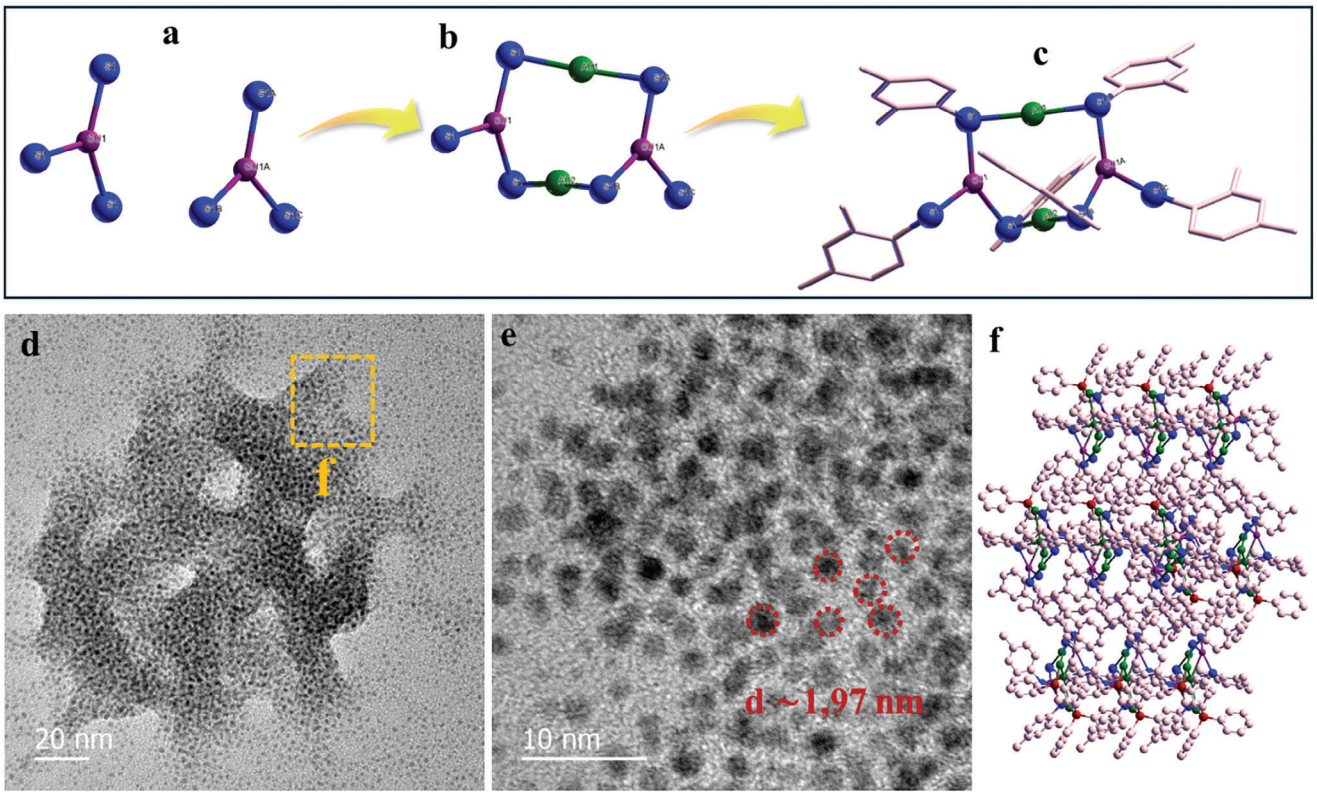

Figure 1. a–c) Anatomy of Au_4Cu_2 NC, d,e) HRTEM of Au_4Cu_2 NC, and f) Packing structure of Au_4Cu_2 NC in single crystal (color labels: green, Au; magenta, Au; blue, S; red, p; pink.

observe that clusters of metal nanoclusters are randomly scattered across the ZIF-8 surface, with each cluster measuring ≈10–20 nm in diameter.

Figure 3c confirms these measurements and reveals the nanoclusters perched precariously on the ZIF-8 substrate, an observation that is made clearer upon further magnification in Figure 3d. Figure 3c further verifies the diameter of the metal nanocluster and we may observe the metal nanocluster loosely attached to the ZIF-8 substrate. Figure 3e–h display the HRTEM/TEM, and scanning transmission electron microscopy (STEM) images of the in situ integrated Au_4Cu_2 NC/ZIF-8. Figure 3e,f indicates an absence of the aforementioned

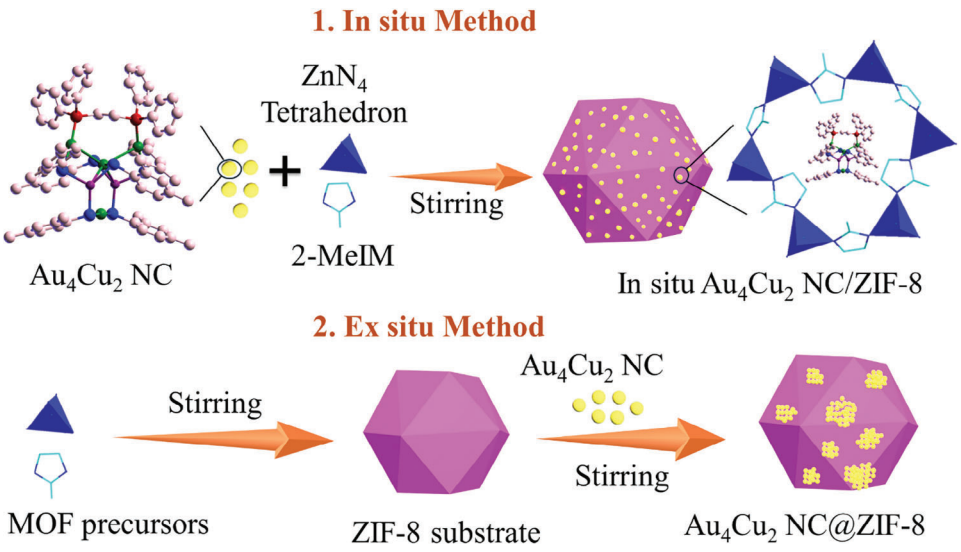

Figure 2. Schematic illustration of in situ integrated Au_4Cu_2 NC/ZIF-8 and ex situ deposited Au_4Cu_2 NC@ZIF-8.

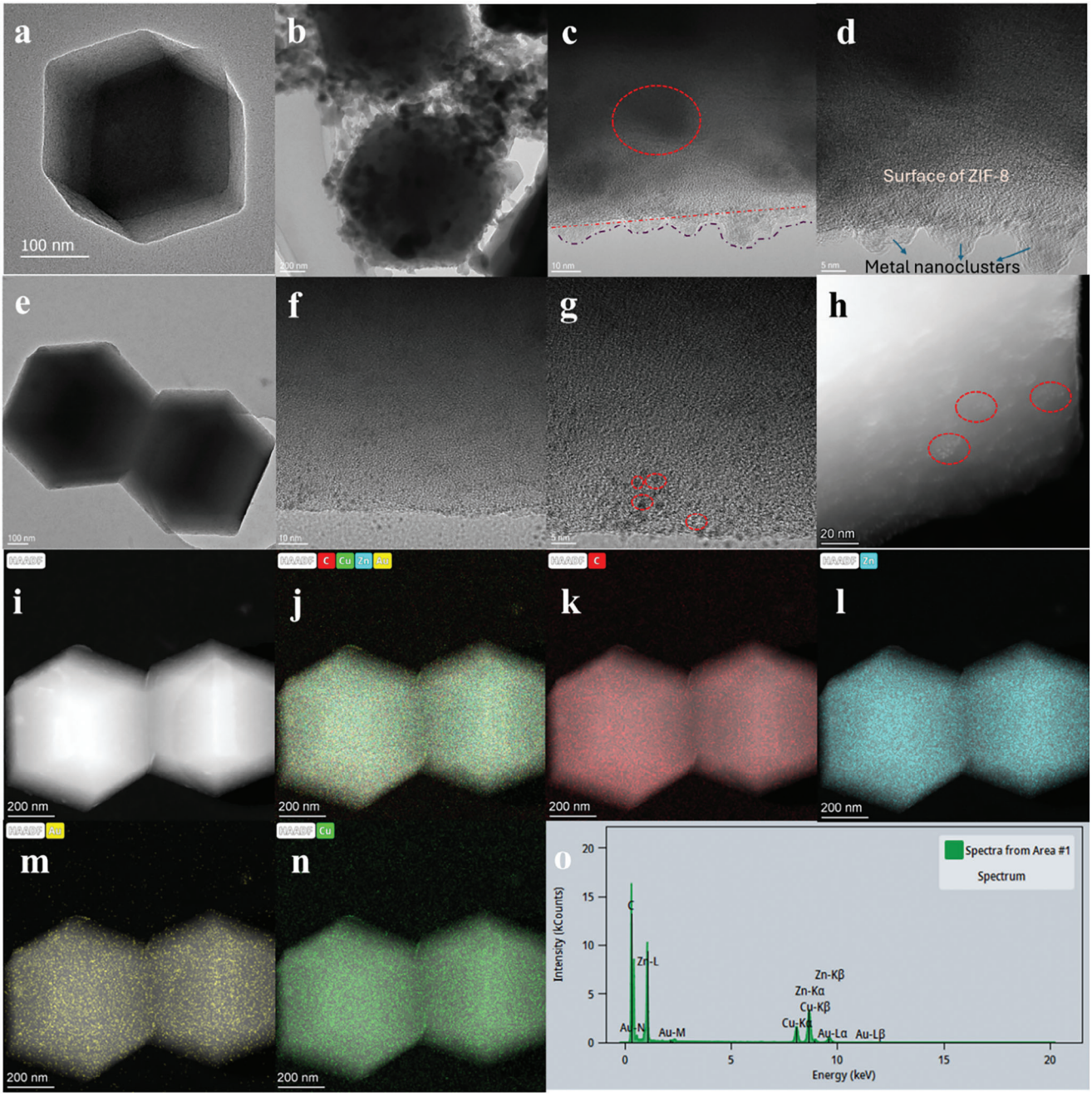

Figure 3. TEM image of a) ZIF-8, b–d) ex situ deposited Au_4Cu_2 NC@ZIF-8, e–g) in situ integrated Au_4Cu_2 NC/ZIF-8, h) STEM, i) HAADF, and j–o) HAADF-EDS images of in situ integrated Au_4Cu_2 NC/ZIF-8.

clumping, and higher magnification images reveal a homogeneous distribution of the metal nanoclusters across the ZIF-8 substrate. Notably, the in situ integration method maintains the nanocluster size under 2 nm, as highlighted in Figure 3g, thereby avoiding the aggregation seen in the ex situ samples. The STEM image in Figure 3h confirms the TEM findings, showcasing the even dispersal of individual nanoclusters on the ZIF-8 substrate. To further affirm these observations, HAADF and HAADF-EDS techniques were employed to in situ integrated Au_4Cu_2 NC/ZIF-8, results shown in Figure 3i–o. These techniques confirmed the homogeneity in the distribution of Au_4Cu_2 NC on ZIF-8 when integrated through in situ method. The elemental maps revealed a consistent spread of gold and copper throughout the ZIF-8 matrix, accompanied by the characteristic signals of zinc and carbon associated with ZIF-8 structure. The in situ integration method ensures a uniform and stable incorporation of metal nanoclusters into the metal–organic framework (MOF) substrate, offering a promising avenue for the synthesis of well-dispersed nanocomposite materials.

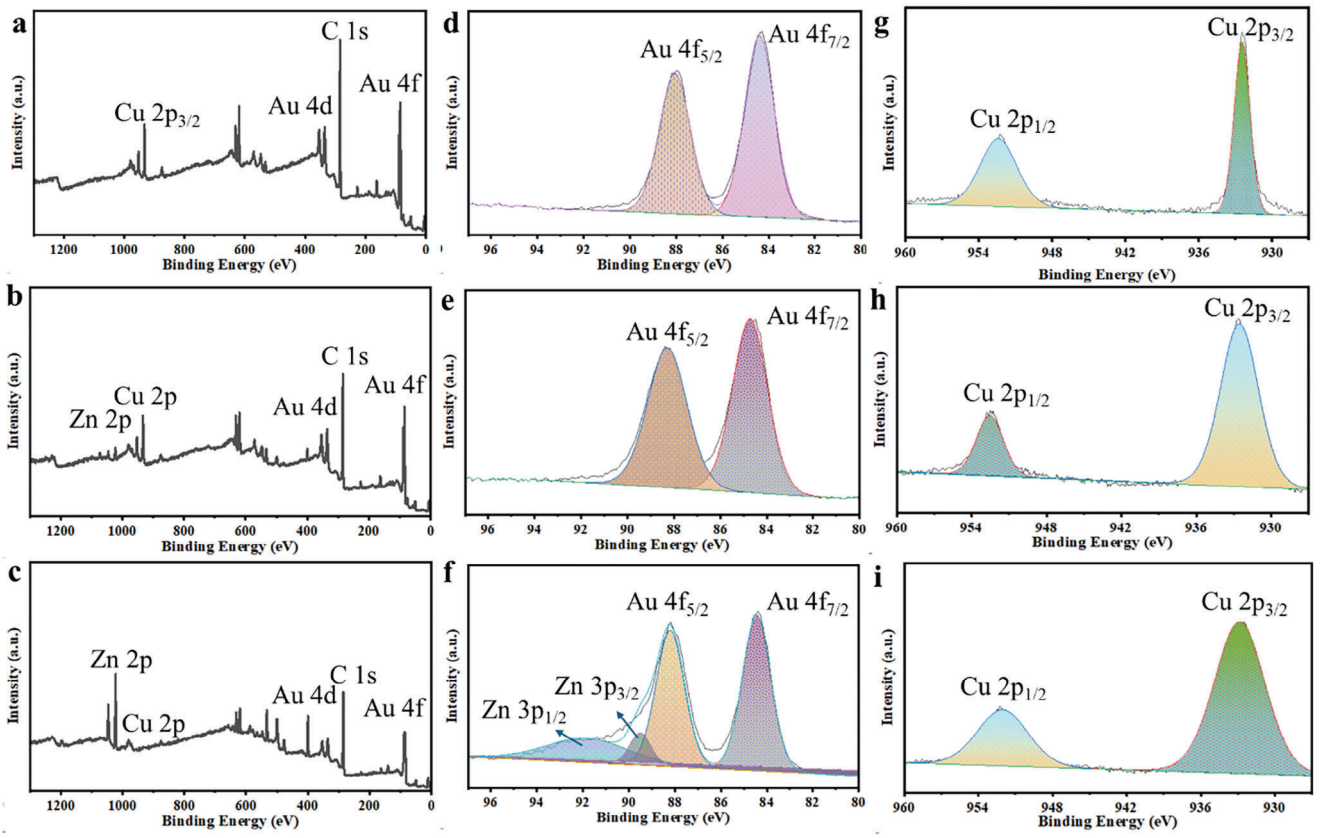

Figure 4. XPS survey of a) Au_4Cu_2 NC, b) ex situ deposited Au_4Cu_2 NC@ZIF-8, c) in situ integrated Au_4Cu_2 NC/ZIF-8. Au 4f XPS of d) Au_4Cu_2 NC, e) ex situ deposited Au_4Cu_2 NC@ZIF-8, f) in situ integrated Au_4Cu_2 NC/ZIF-8. XPS of Cu 2p g) Au_4Cu_2 NC, h) ex situ deposited Au_4Cu_2 NC@ZIF-8, i) in situ integrated Au_4Cu_2 NC/ZIF-8.

Additionally, the stability of the ZIF-8 substrate during the integration process was confirmed through X-ray crystallography (XRD). Figure S2 (Supporting Information) displays the XRD patterns in situ Au_4Cu_2 NC/ZIF-8 and the ZIF-8 substrate. The characteristic peaks at 11°, 13°, 15°, 17°, and 19° attributed to (0 0 2), (1 1 2), (0 2 2), (0 1 3), and (2 2 2) planes of ZIF-8, respectively.[32] The absence of new diffraction peaks from impurities in the XRD pattern for in situ Au_4Cu_2 NC/ZIF-8 indicates that the crystal structure of the ZIF-8 substrate remained intact, demonstrating that the integration of nanoclusters did not alter the fundamental crystal structure of the substrate. The successful decoration of the Au_4Cu_2 NC on ZIF-8 was further analysed by a detailed comparison of X-ray photoelectron spectroscopy (XPS) data of pristine Au_4Cu_2 NC, ex situ deposited Au_4Cu_2 NC@ZIF-8, and in situ integrated Au_4Cu_2 NC/ZIF-8, as depicted in **Figure 4**. Figure 4a–c reveal the XPS survey for the Au_4Cu_2 NC, ex situ deposited Au_4Cu_2 NC @ZIF-8 and in situ integrated Au_4Cu_2 NC@ZIF-8, highlighting the presence of both gold (Au) and copper (Cu) elements in pristine Au_4Cu_2 NC while the survey spectra for the hybrid materials indicate the additional presence of zinc (Zn), which signifies the ZIF-8 framework, alongside the peaks for Au and Cu, confirming the incorporation of the Au_4Cu_2 NC in both procedures. The Au 4f XPS of the Au_4Cu_2 NC and their hybrid counterparts with ZIF-8 shows that the pristine nanoclusters present two distinctive peaks corresponding to Au $4f_{5/2}$ and Au $4f_{7/2}$, shown in Figure 4d–f. This pattern is consistently observed in both ex situ and in situ Au_4Cu_2 NC/ZIF-8 hybrids. However, a slight shift in the Au 4f peaks within the hybrid materials suggests the successful formation of Au_4Cu_2 NC within the ZIF-8 matrix. Interestingly, the in situ integrated Au_4Cu_2 NC/ZIF-8 reveals additional XPS peaks at 95 and 96 eV, attributable to Zn $3p_{1/2}$ and Zn $3p_{3/2}$, respectively. This confirms the successful incorporation of the Au_4Cu_2 NC within the ZIF-8 structure. Conversely, the absence of these peaks in the ex situ sample implies that the metal nanoclusters are merely deposited on the ZIF-8 surface, likely due to Van der Waals forces. The Cu 2p XPS for the Au_4Cu_2 NC, as well as the ex situ and in situ hybrid materials are shown in Figure 4g–i. The peaks at 896 and 894 eV, corresponding to Cu $2p_{1/2}$ and Cu $2p_{3/2}$, remain unchanged in the hybrid materials, indicating that the copper's integrity remains intact regardless of the synthesis method. No change in oxidation state of gold, copper, and zinc suggests the integration was facilitated through electrostatic attractions. The comparative XPS analysis of the Au_4Cu_2 NC and their hybrids with ZIF-8 suggests that the in situ method offers a more robust integration of the metal nanocluster into the ZIF-8 framework, establishing a stronger interaction than that achieved through the ex situ approach.

The electrochemical behaviors of in situ integrated Au_4Cu_2 NC/ZIF-8 and ex situ deposited Au_4Cu_2 NC@ZIF-8, were

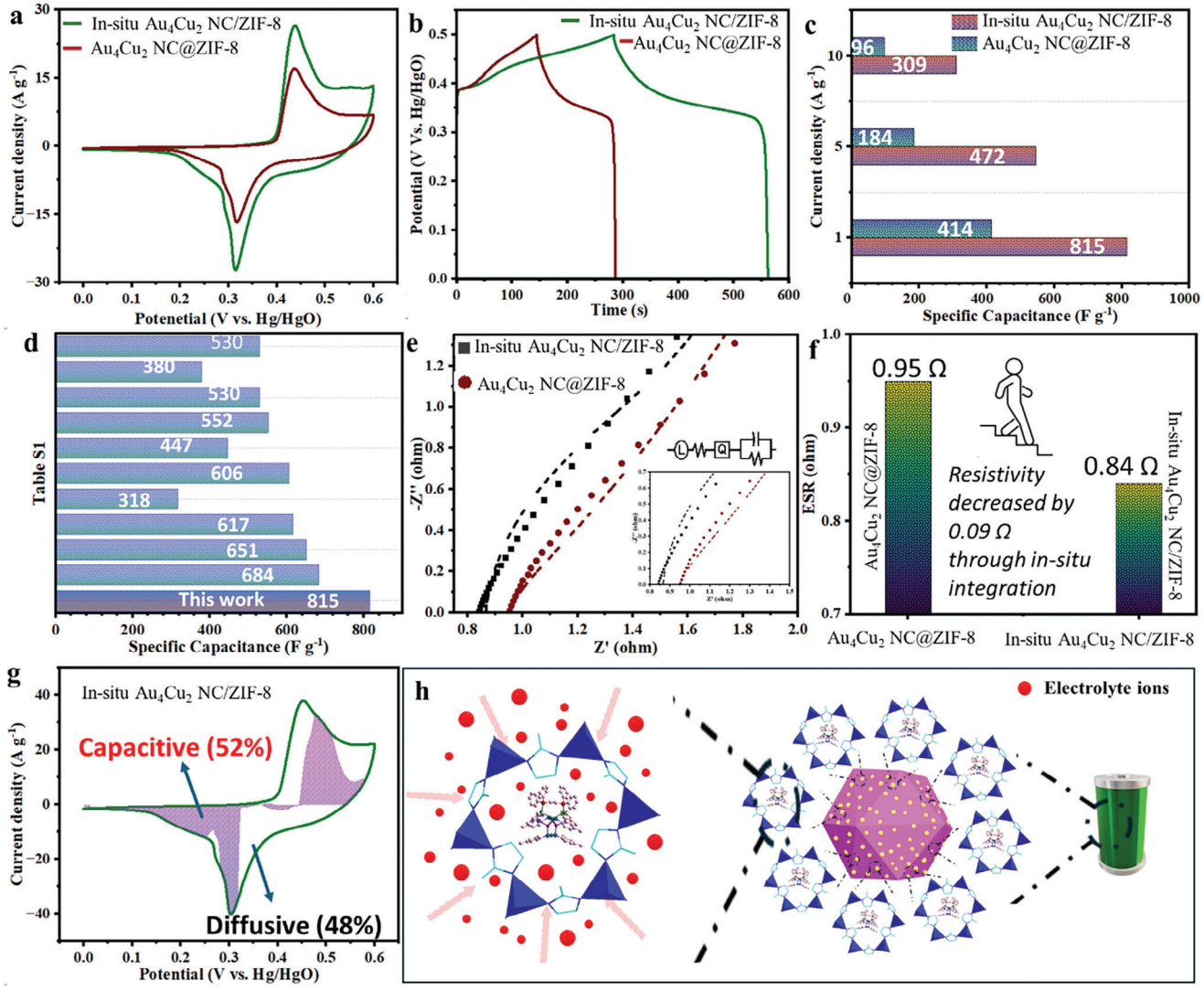

Figure 5. Comparison of in situ Au_4Cu_2 NC/ZIF-8 and Au_4Cu_2 NC@ZIF-8 of a) CV plots at 5 mV s^{-1} and b) GCD plots at current density of 1 A g^{-1}. c) Comparison of specific capacitance of in situ Au_4Cu_2 NC/ZIF-8 and Au_4Cu_2 NC@ZIF-8 at 1, 5, and 10 A g^{-1}. d) Comparison of specific capacitance of in situ Au_4Cu_2 NC/ZIF-8 to reported literature Table S1 (Supporting Information). e) Nyquist plot of in situ Au_4Cu_2 NC/ZIF-8 and Au_4Cu_2 NC@ZIF-8. f) EIS resistance comparison of in situ Au_4Cu_2 NC/ZIF-8 and Au_4Cu_2 NC@ZIF-8. g) Evaluation of capacity contribution of in situ Au_4Cu_2 NC/ZIF-8. h) Illustration of functional principles of in situ Au_4Cu_2 NC/ZIF-8 as an efficient electrode material.

systematically investigated via a three-electrode configuration employing an aqueous 3 M KOH solution as the electrolyte, shown in **Figure 5**. In Figure 5a, the cyclic voltammograms (CV) of the in situ integrated Au_4Cu_2 NC/ZIF-8 and ex situ deposited Au_4Cu_2 NC@ZIF-8 are compared at a scan rate of 5 mV s^{-1} within an established potential window ranging from 0 to 0.6 V. The emergence of two redox peaks for both the in situ and ex situ Au_4Cu_2 nanocluster signifies their Faradaic activity, which is indicative of the presence of multiple oxidation states.[33] Notably, the CV profile for the in situ integrated Au_4Cu_2 NC/ZIF-8 displays a substantially larger area under the curve than that of the ex situ counterpart. This larger area is directly associated with enhanced capacitance compared to the other two electrodes. Figure 5b presents a comparative analysis of galvanostatic charge-discharge (GCD) curves for the in situ integrated Au_4Cu_2 NC/ZIF-8 in relation to the ex situ deposited Au_4Cu_2 NC@ZIF-8. This is performed at a current density of 1 A g^{-1} within a potential range from 0 to 0.5 V. The in situ integrated Au_4Cu_2 NC/ZIF-8 demonstrates a more extensive discharge region and longer discharge duration, reflecting a higher specific capacity than the ex situ prepared Au_4Cu_2 NC@ZIF-8, in alignment with the CV findings. The specific capacities for each material were calculated using equation, reported somewhere else[34] and compared at a current density of 1, 5 and 10 A g^{-1}, as depicted in Figure 5c. A detailed comparison of specific capacitance of both materials from 1 to 10 A g^{-1} is shown in Figure S4 (Supporting Information). The in situ integrated Au_4Cu_2 NC/ZIF-8 and the ex situ deposited Au_4Cu_2 NC@ZIF demonstrated specific capacitances of 815 and 414 F g^{-1}, respectively, at a current density of 1 A g^{-1}, as illustrated in Figure 5c. The specific capacitance of the hybrid

electrode was further increased by two times following the in situ integration of Au_4Cu_2 NC. A comprehensive comparison of the in situ integrated Au_4Cu_2 NC/ZIF-8 electrode with other previously reported electrode materials is summarized in Table S1 (Supporting Information), Figure 5d. Further, we have calculated the specific capacity for electrode material and the in situ integrated Au_4Cu_2 NC/ZIF-8 and the ex situ deposited Au_4Cu_2 NC@ZIF demonstrated specific capacity of 113 and 57 mAh g^{-1}, respectively, at a current density of 1 A g^{-1}, as calculated through reported literature.[33]

The electrochemical impedance spectroscopy (EIS) data for the both electrode materials, in situ integrated Au_4Cu_2 NC/ZIF-8, and ex situ deposited Au_4Cu_2 NC@ZIF-8 were thoroughly analyzed at a frequency ranging from 100 kHz to 0.01 Hz and depicted in Figure 5e. The equivalent series resistance (ESR), which is identified as the intercept on the real axis at the high-frequency end, represents the solution resistance.[35–37] This resistance is related to the resistivity of the active electrode material, the electrolyte, and the connection between the active material and the current collector.[38–40] Meanwhile, a straight line at the low-frequency end indicates Warburg resistance, which is a measure of the impedance at the electrode/electrolyte interface and the diffusion of electrolyte ions within the electrode material's surface and pores, reflecting capacitive behavior.[41] When compared to the ex situ deposited Au_4Cu_2 NC@ZIF-8 (ESR ≈0.95 ohm) and in situ integrated Au_4Cu_2 NC/ZIF-8 (ESR ≈0.84 ohm) showcased a lower ESR value of 0.09 ohm, confirming its diminished resistance and superior electrical conductivity, shown in Figure 5e,f. The strategic incorporation of specific atoms into the ex situ Au_4Cu_2 NC structure reduces the electrode material's resistance and enhances conductivity, which can be attributed to the induced structural distortion.

CV detailed for the in situ integrated Au_4Cu_2 NC/ZIF-8 and Au_4Cu_2 NC@ZIF-8 were recorded at varying scan rates ranging from 1 to 50 mV s^{-1}, as showcased in Figure S3a,b (Supporting Information). The area under the current density peaks, indicative of redox activity, was observed to increase with the scan rate escalation from 1 to 50 mV s^{-1}. Correspondingly, the cathodic and anodic peaks of the in situ integrated Au_4Cu_2 NC/ZIF-8 shifted toward more negative and more positive potentials, respectively. This shift denotes the polarization of the metal nanoclusters, augmenting ion and electron transfer rates, a pattern that was consistent with the other electrode materials. The maintenance of symmetrical CV profiles at high scan rates suggests accelerated redox reactions, enhanced electrochemical reversibility, and effective rate capabilities.[2,42,43] Figure S3c,d (Supporting Information) displays the comprehensive galvanostatic charge-discharge (GCD) curves (1–10 A g^{-1}) of the in situ integrated Au_4Cu_2 NC/ZIF-8 and ex situ deposited Au_4Cu_2 NC@ZIF-8 electrode, respectively. The effectiveness of electrode materials significantly depends on their ability to sustain performance throughout numerous charge-discharge cycles. To evaluate this, the electrodes were subjected to a cycling test consisting of 10 000 galvanostatic charge-discharge (GCD) cycles at a current density of 10 A g^{-1}, as shown in Figure S5 (Supporting Information). The outcomes reveal that the electrodes retained 99.5% Coulombic efficiency and preserved 91% of their initial capacity. The remarkable capacity retention of electrode material associated with the MOF counterpart.

To elucidate the charge storage mechanism, the proportion of the current in the in situ integrated Au_4Cu_2 NC/ZIF-8 electrode arising from diffusion-controlled and surface-limited processes was examined based on the CV profiles. b value calculated for the in situ integrated Au_4Cu_2 NC/ZIF-8 was found to be 0.71. This suggests that the predominant charge storage mechanism leans toward a both capacitive and diffusion-controlled process (Figure 5g). The presence of both battery and pseudocapacitive characteristics within the in situ integrated Au_4Cu_2 NC/ZIF-8 electrode material contributes to enhanced overall electrochemical performance. The superior electrochemical performance of the in situ integrated Au_4Cu_2 NC/ZIF-8 electrode material can be attributed to following factors: First, the uniform distribution of metal nanoclusters on the MOF surface creates a strategy that enhances the number of active sites. Second, the incorporation of bi-metals in these nanoclusters creates a synergistic effect that significantly improves the properties of the electrode material. Additionally, the in situ method of decorating the MOF enhances the conductivity of the substrate, which in turn substantially increases the specific capacitance of the material. Illustration of functional principles of in situ Au_4Cu_2 NC/ZIF-8 charge storage mechanism shown in Figure 5h.

To assess the potential of the in situ integrated Au_4Cu_2 NC/ZIF-8 as an electrode material for practical applications, it was incorporated into a hybrid supercapacitor (HSC). The HSC was assembled with activated carbon (AC) serving as the negative electrode, as outlined in previous studies,[39] while the in situ integrated Au_4Cu_2 NC/ZIF-8 functioned as the positive electrode, with a 3 M KOH solution acting as the electrolyte. The device was configured to balance the charge between electrodes according to Equation S1 (Supporting Information).

Figure 6a presents the schematic representation of the assembled hybrid device. As depicted in Figure 6b, the CV profiles for AC and the in situ integrated Au_4Cu_2 NC/ZIF-8 were obtained at a scan rate of 10 mV s^{-1}. The AC displayed an outstanding electric double-layer capacitive (EDLC) response, whereas the in situ integrated Au_4Cu_2 NC/ZIF-8 exhibited a Faradaic charge storage mechanism. A thorough examination of the CV curves at various scan rates, also shown in Figure 6c, confirmed that the HSC could operate stably at a voltage of 1.6 V. The GCD curves, detailed in Figure 6d, validate a consistent potential window for the asymmetric cell across varying current densities from 1 to 10 A g^{-1}. Moreover, the energy density and power density of the HSC were computed using Equations S6 and S7 (Supporting Information), respectively.

The HCS, comprising the in situ integrated Au_4Cu_2 NC/ZIF-8 in conjunction with AC, achieved an impressive power density of 1474 W kg^{-1} at an energy density of 87.2 Wh kg^{-1}. A comparative analysis of the power and energy densities of the in situ integrated Au_4Cu_2 NC/ZIF-8//AC cell with other documented devices is depicted in the Ragone plot (Figure 6e) and summarized in Table S2 (Supporting Information). Further, the HSC device was subjected to a cycling test consisting of 8000 galvanostatic charge-discharge (GCD) cycles at a current density of 5 A g^{-1}, as shown in Figure S6 (Supporting Information). The outcomes reveal that the electrodes retained 99.9% Coulombic efficiency and preserved 68% of their initial capacity. An inset in Figure 6e illustrates the capability of two serially connected HSCs to power

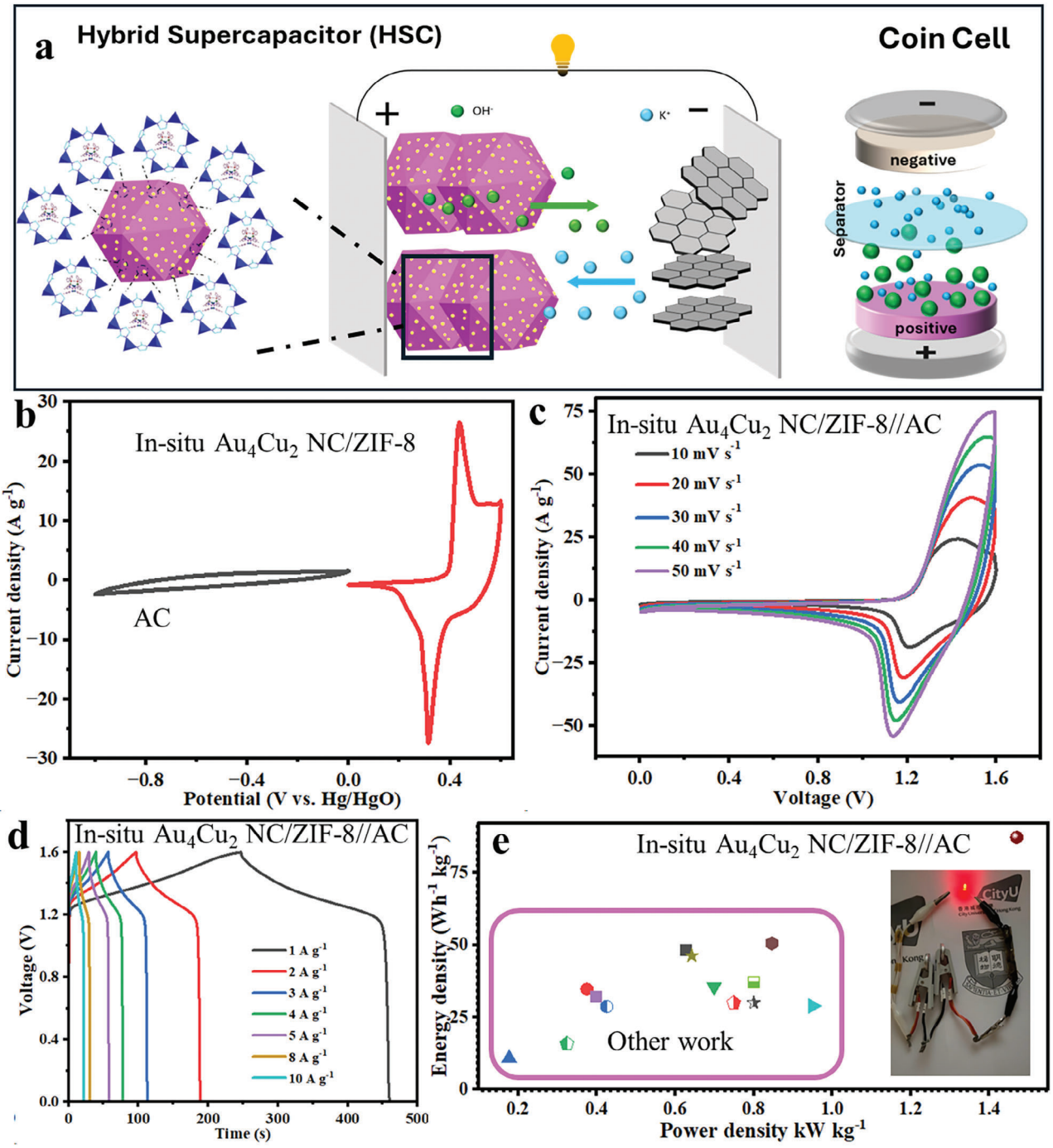

Figure 6. a) Schematic illustration of the in situ Au_4Cu_2 NC/ZIF-8//AC based HSC device configuration (positive electrode) and coin cell b) Preliminary CV curve comparison of AC and in situ Au_4Cu_2 NC/ZIF-8 in three-electrode measurements system at 10 mV s^{-1}. Detailed c) CV plots from 1 to 50 mV s^{-1}, and d) GCD curves of in situ Au_4Cu_2 NC/ZIF-8//AC HSC at current density 1–10 A g^{-1}. e) Ragone plot of the HSC device; inset: illumination of LEDs.

a red LED, demonstrating the practical viability of the in situ integrated Au_4Cu_2 NC/ZIF-8 electrode material.

3. Conclusion

In conclusion, we have successfully integrated atomically precise bimetallic Au_4Cu_2 nanoclusters onto ZIF-8 using an in situ method. This approach was validated by morphological analysis and confirmed the excellent uniform distribution of nanoclusters in the in situ Au_4Cu_2 NC/ZIF-8 compared to the ex situ deposited Au_4Cu_2 NC@ZIF-8. The in situ Au_4Cu_2 NC/ZIF-8 exhibited the remarkable specific capacitance of 815 F g^{-1} (two times higher than ex situ Au_4Cu_2 NC@ZIF-8) at a current density of 1 A g^{-1}. The higher specific capacitance of in situ Au_4Cu_2 NC/ZIF-8

electrode material refers to excellent morphological characteristics and remarkable conductivity. Further, in practical applications, this electrode demonstrated an energy density of 87.2 Wh kg^{-1} at a power density of 1474 W kg^{-1}, highlighting its robustness and potential for high-performance energy storage applications. Our findings demonstrate that this in situ integration method effectively prevents nanocluster aggregation on the substrate, addressing a major challenge in supercapacitor development. The synthesis route of in situ Au_4Cu_2 NC/ZIF-8 represents a significant advancement toward more efficient and sustainable supercapacitor electrode material.

Supporting Information

Supporting Information is available from the Wiley Online Library or from the author.

Acknowledgements

The authors gratefully acknowledge The University of Hong Kong, the Research Grants Council of the Hong Kong Special Administrative Region, People's Republic of China (RGC: 27301820 and 17313922), the Croucher Foundation, the Innovation and Technology Commission (HKSAR, China), the National Natural Science Foundation of China (No. 22201236) and Donations for Research Projects_RMGS (project number 9229006) and for their financial support. This work was also supported by the Hong Kong Research Grants Council (Project Number CityU 11218420).

Conflict of Interest

The authors declare no conflict of interest.

Data Availability Statement

The data that support the findings of this study are available from the corresponding author upon reasonable request.

Keywords

energy storage devices, hybrid supercapacitor, metal nanoclusters, MOF, supercapacitor

Received: April 25, 2024
Revised: July 15, 2024
Published online: July 22, 2024

[1] I. Hussain, S. Iqbal, C. Lamiel, A. Alfantazi, K. Zhang, *J. Mater. Chem. A* **2022**, *10*, 4475.
[2] I. Hussain, S. Iqbal, T. Hussain, Y. Chen, M. Ahmad, M. S. Javed, A. AlFantazi, K. Zhang, *J. Mater. Chem. A* **2021**, *9*, 17790.
[3] S. Gu, R. Hao, J. Chen, X. Chen, K. Liu, I. Hussain, G. Liu, Z. Wang, Q. Gan, H. Guo, *Mater. Chem. Front.* **2022**, *6*, 2545.
[4] L. Wang, Y. Han, X. Feng, J. Zhou, P. Qi, B. Wang, *Coord. Chem. Rev.* **2016**, *307*, 361.
[5] R. R. Salunkhe, Y. V. Kaneti, Y. Yamauchi, *ACS Nano* **2017**, *11*, 5293.
[6] N. Raza, T. Kumar, V. Singh, K.-H. Kim, *Coord. Chem. Rev.* **2021**, *430*, 213660.
[7] H. Wang, Q.-L. Zhu, R. Zou, Q. Xu, *Chem* **2017**, *2*, 52.
[8] S. Kuyuldar, D. T. Genna, C. Burda, *J. Mater. Chem. A* **2019**, *7*, 21545.
[9] Y. Zhao, Z. Song, X. Li, Q. Sun, N. Cheng, S. Lawes, X. Sun, *Energy Storage Mater.* **2016**, *2*, 35.
[10] I. Chakraborty, T. Pradeep, *Chem. Rev.* **2017**, *117*, 8208.
[11] R. Jin, C. Zeng, M. Zhou, Y. Chen, *Chem. Rev.* **2016**, *116*, 10346.
[12] X. Kang, H. Chong, M. Zhu, *Nanoscale* **2018**, *10*, 10758.
[13] Z. Lei, X.-K. Wan, S.-F. Yuan, Z.-J. Guan, Q.-M. Wang, *Acc. Chem. Res.* **2018**, *51*, 2465.
[14] R. Jin, *Nanoscale* **2015**, *7*, 1549.
[15] X. Kang, M. Zhu, *Chem. Soc. Rev.* **2019**, *48*, 2422.
[16] Y.-L. Li, Z.-Y. Wang, X.-H. Ma, P. Luo, C.-X. Du, S.-Q. Zang, *Nanoscale* **2019**, *11*, 5151.
[17] S. Knoppe, T. Bürgi, *Acc. Chem. Res.* **2014**, *47*, 1318.
[18] Y. Li, T. Higaki, X. Du, R. Jin, *Adv. Mater.* **2020**, *32*, 1905488.
[19] S. Li, Z. P. Yan, X. L. Li, Y. J. Kong, H. Y. Li, G. G. Gao, Y. X. Zheng, S. Q. Zang, *Adv. Sci.* **2020**, *7*, 2000738.
[20] M.-M. Zhang, X.-Y. Dong, Z.-Y. Wang, X.-M. Luo, J.-H. Huang, S.-Q. Zang, T. C. Mak, *J. Am. Chem. Soc.* **2021**, *143*, 6048.
[21] Z. Han, X.-Y. Dong, P. Luo, S. Li, Z.-Y. Wang, S.-Q. Zang, T. C. Mak, *Sci. Adv.* **2020**, *6*, eaay0107.
[22] X. Du, R. Jin, *ACS Nano* **2019**, *13*, 7383.
[23] T. Higaki, Y. Li, S. Zhao, Q. Li, S. Li, X. S. Du, S. Yang, J. Chai, R. Jin, *Angew. Chem.* **2019**, *131*, 8377.
[24] Y. Du, H. Sheng, D. Astruc, M. Zhu, *Chem. Rev.* **2019**, *120*, 526.
[25] H. Qian, W. T. Eckenhoff, Y. Zhu, T. Pintauer, R. Jin, *J. Am. Chem. Soc.* **2010**, *132*, 8280.
[26] A. Ghosh, O. F. Mohammed, O. M. Bakr, *Acc. Chem. Res.* **2018**, *51*, 3094.
[27] S. Hossain, Y. Niihori, L. V. Nair, B. Kumar, W. Kurashige, Y. Negishi, *Acc. Chem. Res* **2018**, *51*, 3114.
[28] G. Chu, C. Zhang, Y. Liu, Z. Cao, L. Wang, Y. Chen, W. Zhou, G. Gao, K. Wang, D. Cui, *ACS Nano* **2020**, *14*, 15633.
[29] E. Fernández, M. Boronat, *J. Phys.: Condens. Matter* **2018**, *31*, 013002.
[30] Y. Luo, S. Fan, W. Yu, Z. Wu, D. A. Cullen, C. Liang, J. Shi, C. Su, *Adv. Mater.* **2018**, *30*, 1704576.
[31] L. Sun, Y. Yun, H. Sheng, Y. Du, Y. Ding, P. Wu, P. Li, M. Zhu, *J. Mater. Chem. A* **2018**, *6*, 15371.
[32] X. Liu, L. He, J. Zheng, J. Guo, F. Bi, X. Ma, K. Zhao, Y. Liu, R. Song, Z. Tang, *Adv. Mater.* **2015**, *27*, 3273.
[33] I. Hussain, S. Sahoo, D. Mohapatra, M. Ahmad, S. Iqbal, M. S. Javed, S. Gu, N. Qin, C. Lamiel, K. Zhang, *Appl. Mater. Today* **2022**, *26*, 101297.
[34] T. Nawaz, M. Ahmad, M. Z. Ansari, I. Hussain, X. Chen, L.-J. Liu, R. Walia, K. H. Low, S. Zhuang, K. Zhang, *Chem. Eng. J.* **2023**, *468*, 143575.
[35] N. Li, X. Zhang, S. Zhao, C. Li, X. Li, T. Wang, Y. Xing, G. Qu, X. Xu, *Chin. Chem. Lett.* **2023**, *34*, 107669.
[36] C. Wang, X. Ji, J. Liang, S. Zhao, X. Zhang, G. Qu, W. Shao, C. Li, G. Zhao, X. Xu, *Angew. Chem., Int. Ed.* **2024**, 202409271.
[37] T. Li, S. Hu, C. Wang, D. Wang, M. Xu, C. Chang, X. Xu, C. Han, *Angew. Chem., Int. Ed.* **2023**, *62*, 202314883.
[38] I. Hussain, J. M. Lee, S. Iqbal, H. S. Kim, S. W. Jang, J. Y. Jung, H. J. An, C. Lamiel, S. G. Mohamed, Y. R. Lee, *Electrochim. Acta* **2020**, *340*, 135953.
[39] I. Hussain, T. Hussain, C. Lamiel, K. Zhang, *J. Power Sources* **2020**, *480*, 228873.

[40] I. Hussain, S. Iqbal, T. Hussain, W. L. Cheung, S. A. Khan, J. Zhou, M. Ahmad, S. A. Khan, C. Lamiel, M. Imran, A. AlFantazi, K. Zhang, *Mater. Today Phys.* **2022**, *23*, 100655.
[41] M. Manikandan, K. Subramani, S. Dhanuskodi, M. Sathish, *Energy Fuels* **2021**, *35*, 12527.
[42] M. Ahmad, I. Hussain, T. Nawaz, Y. Li, X. Chen, S. Ali, M. Imran, X. Ma, K. Zhang, *J. Power Sources* **2022**, *534*, 231414.
[43] I. Hussain, T. Hussain, S. B. Ahmed, T. Kaewmaraya, M. Ahmad, X. Chen, M. S. Javed, C. Lamiel, K. Zhang, *J. Power Sources* **2021**, *513*, 230556.